FISEVIER

Contents lists available at ScienceDirect

Acta Biomaterialia

journal homepage: www.elsevier.com/locate/actbio



Full length article

Fatigue behavior of biodegradable Zn-Li binary alloys in air and simulated body fluid with pure Zn as control



Guannan Li^a, Dafu Chen^{b,**}, Yoji Mine^c, Kazuki Takashima^c, Yufeng Zheng^{a,*}

- ^a School of Materials Science and Engineering, Peking University, Beijing, 100871, China
- b Laboratory of Bone Tissue Engineering, Beijing Research Institute of Traumatology and Orthopaedics, Beijing JiShuiTan Hospital, Beijing 100035, China
- ^c Department of Materials Science and Engineering, Kumamoto University, 2–39–1 Kurokami, Chuo-ku, Kumamoto 860-8555, Japan

ARTICLE INFO

Article history:
Received 5 April 2023
Revised 4 July 2023
Accepted 20 July 2023
Available online 28 July 2023

Keywords: Biodegradable metals Zn-Li alloys Corrosion fatigue Air Simulated body fluid

ABSTRACT

Zn-Li-based alloys have drawn great attention as promising candidates for load-bearing sites, such as intramedullary nails and bone plates. They possess high monotonic strength (over 500MPa) and better pitting resistance with lithium-rich layers acting as barriers for corrosion attack under (quasi-)static conditions. However, their response to dynamic loadings such as fatigue is still unknown. Herein, the corrosion fatigue behavior of a series of Zn-Li binary alloys with different lithium addition amounts was tested in simulated body fluid. Tensile and fatigue strength of the materials were proportional to lithium content while corrosion fatigue strength was not. Extremely long cracks that extended parallel to the loading direction were found in Zn-1.0wt.%Li alloys. These cracks propagated by selective dissolution of the lithium-rich phase in the eutectoid regions and drastically reduced the corrosion fatigue strength of Zn-1.0wt.%Li alloy owing to exacerbated crack propagation. To sum up, Zn-Li binary alloys showed fatigue strength comparable to pure iron and pure titanium, which confirmed their loading capacity under dynamic conditions.

Statement of significance

Zn-Li-based alloys are qualified as biodegradable metals and are dedicated to load-bearing applications. Current research has shown that lithium can suppress pitting corrosion by the formation of lithium-rich layers on the alloy surface during (quasi-)static conditions. However, how these materials respond to dynamic loading is still unknown. The present study investigated the influence of lithium amount (0.1~1.0wt.%) on the corrosion fatigue behavior of binary Zn-Li alloys. The results showed that lithium effectively improved the mechanical strength but can harm corrosion fatigue strength at high content due to selective dissolution of lithium-rich phase. This demonstrated that the amount of lithium should be controlled for optimal properties. Zn-0.8wt.%Li alloy demonstrated a good combination of tensile and corrosion fatigue strength, which can be further improved by proper alloying and thermomechanical treatment.

© 2023 Acta Materialia Inc. Published by Elsevier Ltd. All rights reserved.

1. Introduction

Biodegradable metals are a new generation of metallic biomaterials that aimed to eliminate the drawbacks of nondegradable metallic materials, such as chronic inflammation and secondary surgery [1–3]. After decades of development, Zn-based biodegrad-

E-mail addresses: chendafujst@126.com (D. Chen), yfzheng@pku.edu.cn (Y. Zheng).

able metals have been proven to be one of the most potential candidates owing to their proper biodegradability and acceptable biocompatibility [4–8]. Zn-Li based alloys possess the highest strength among all kinds of Zn-based biodegradable metals and meanwhile have tunable degradation behavior, which makes them ideal materials for load-bearing applications, such as intramedullary nails and bone plates [6,9–14].

Fatigue describes the crack initiation, propagation, and final fracture induced by the cyclic loading of a structure [15]. Under such circumstances, materials usually fail at a stress amplitude much lower than their yield stress. Fatigue is common for structures in aircraft, offshore platforms, railways, and nuclear power

^{*} Corresponding author at: School of Materials Science and Engineering, Peking University, No. 5 Yi-He-Yuan Road, Hai-Dian District, Beijing 100871, China.

^{**} Corresponding author.

plants. In the biomedical field, implants, particularly orthopedic devices, are prone to corrosion fatigue during service [16]. Thus, implant materials must have high fatigue resistance in the physiological environment.

Two methods are normally applied for investigating the fatigue behaviors of metallic materials: Cumulative Fatigue Damage (CFD) and Fatigue Crack Propagation (FCP) [17]. The former method uses the S-N curve (Stress Amplitude-Number of cycles to failure) for predicting the fatigue life of a sample, while the latter focuses on the crack propagation speed on a microscopic scale. Processing history, surface roughness, and service environment all influence the corrosion fatigue property of a material [18]. For nondegradable metallic biomaterials, Co-based alloys normally possess the best fatigue strength, followed by Ti-6Al-4V and 316SS [19]. Biodegradable metals, on the other hand, do not own that high corrosion fatigue strength considering their biodegradability. The concern thus shifts to the durability of their mechanical integrity. Gu et al. studied the fatigue behaviors of as-cast AZ91D and asextruded WE43 alloys [20]. The corrosion fatigue strength was calculated to be 20MPa and 40MPa, respectively. Cracks were found to initiate from corrosion pits. Jafari et al. came up with similar conclusions and determined that the crack propagated in a transgranular manner by hydrogen embrittlement [21]. Bian et al. investigated the corrosion fatigue behaviors of pure magnesium, Mg-1Ca, and Mg-2Zn-0.2Ca in simulated body fluid (SBF) [22]. The corresponding fatigue strength was calculated. Han et al. studied the corrosion fatigue of AZ31B under various loading frequencies and found that the stress and corrosion coupled more intensely under higher frequencies [23]. Li et al. studied the corrosion fatigue property of additively manufactured pure iron and found its corrosion fatigue strength to be 65% of its fatigue strength in the air [24].

For industrial and biomedical zinc alloys, the number of such research stays low. Fegredo et al. investigated the influence of grain size and surface condition on the fatigue strength of pure zinc [25,26]. Their results showed that finer grains and surface deformation twins induced by processing benefited the fatigue strength. In addition, fatigue cracks were found to propagate in an intergranular manner at or above room temperature. Tanaka et al. found that compared to a mixed microstructure, a pure equiaxed structure led to prolonged fatigue life in Zn-22Al alloys [27]. For biomedical zinc alloys, Li et al. found that the corrosion fatigue strength of an additively manufactured pure zinc stent reached 80% of its fatigue strength in the air [28]. Li et al. tested and calculated the fatigue and corrosion fatigue strength of Zn-0.8wt.%Li and Zn-2.0wt.%Cu-0.8wt.%Li alloys as 65MPa and 80MPa, respectively, based on a relatively short fatigue life of 5.6 × 10⁵ cycles [29].

Researchers have shown that the addition of lithium can lead to a series of variations in phase and microstructure [11]. The resulted ${\rm Zn+\alpha-LiZn_4}$ eutectoid structure enhanced the mechanical properties. Herein, we formulated Zn-Li binary alloys with various compositions and performed tension-compression fatigue tests both in the air and in simulated body fluid. The fatigue strengths were determined and compared with previous results of biodegradable alloys. We elucidated the crack-propagating mechanisms with the help of metallography, fractography, Electron Backscattered Diffraction (EBSD) and Transmission Electron Microscope (TEM). Thereafter the crack propagation mechanism was discussed.

2. Materials and methods

2.1. Materials and specimen preparation

The nominal compositions of the investigated materials were pure zinc (99.99wt.%) and Zn-xLi (x=0.1, 0.4, 0.8, and 1.0 weight percentages, respectively). The as-cast ingots were homogenized at 300°C for 1.5 hours in a nitrogen atmosphere. The ingots were then

kept at 200°C for 10 minutes followed by extrusion to a diameter of 10mm with a speed of 1mm/s (the extrusion ratio was 16:1) and air cooling to ambient temperature. Dogbone specimens for tensile tests, cylindrical specimens for compressive tests, and fatigue specimens with a circular cross-section were all machined and loaded parallel to the extrusion direction.

2.2. Microstructural characterization and phase identification

Mechanical polishing was performed on SiC abrasive papers from 400 grit to 2000 grit gradually until mirror-like surfaces were achieved. The samples were then electropolished for EBSD tests in Scanning Electron Microscope (SEM). The experiments were conducted on JSM-7200F, and data analysis was conducted via Channel 5 software. XRD analysis was applied for phase identification on Rigaku DMAX 2400 which used Cu K α radiation. The tests were operated at 40 kV and 100 mA with a scanning rate of 4°/min and a test range of 10°-90°.

2.3. Monotonic mechanical tests

The monotonic mechanical tests were carried out at an initial strain rate of 0.001/s under ambient temperature on a universal material testing machine (Instron 5969). Three parallel measurements were taken for each material. Tension dogbone specimens had a gauge length of 25mm, a width of 6mm, and a thickness of 2.5mm. The compression specimens were cylindrical with a diameter of 5mm and a height of 7.5mm.

2.4. Fatigue tests in air and SBF

Fatigue tests were conducted on an all-electric dynamic test instrument (Instron E3000) under axial sinusoidal loading. The operating mode was a fully reversed fatigue test with a stress ratio of R=-1 and a frequency of 10Hz. The stress-controlled fatigue tests were continued until failure of the sample or until 1 \times 10 7 cycles were reached.

2.5. Fracture surface analysis and crack morphology

The fatigue fracture surfaces of samples that failed at over one million cycles were observed under an SEM (Hitachi S-4800). For better observation, the corrosion products were removed using hot chromic acid. According to ASTM G1-03, 200g chromium trioxide was added to reagent water to make 1000mL solution. The resulted chromic acid was then heated to 80°C and the fractured samples were rinsed for 1min in it. Thereafter, samples were mounted in conductive resin and polished to reveal the crack morphology inside the substrate.

2.6. EBSD analysis around crack tips

To demonstrate the crack propagation mechanism, samples with corrosion fatigue cracks of interest were electropolished and analyzed using EBSD. Electropolishing was conducted under room temperature in a solution containing 33 vol% orthophosphoric acid and 67 vol% ethanol at an applied voltage of 3V. A scanning step size of a tenth of the average grain size was applied during EBSD.

2.7. TEM analysis of fatigued microstructure

The microstructure after cyclic loading was characterized under TEM (FEI Talos F200X) for Zn-0.8wt.%Li alloy. Samples were first electropolished using 4% perchloric acid in ethanol at -35°C (Struers Tenupol-5) and then ion-polished (Gatan 691) for better image quality.

2.8. Statistical analysis

Data from tension, compression, and fatigue tests were presented as mean \pm standard deviation (n = 3 for tension and fatigue, n=4 for compression, independent samples). Fatigue strength and fatigue limit values were calculated using linear regression method according to measured data points (n = 18, independent samples). The grain size data were obtained through a built-in program of Channel 5 software and were presented as mean \pm standard deviation. For each material, over 100 grains were included.

3. Results

3.1. Microstructure and phases

Fig. 1 shows the XRD patterns of the investigated biodegradable metals. For pure zinc sample, data analysis confirmed the existence of the Zn phase (PDF card No.04-005-9306). Another α -LiZn₄ phase [30] was confirmed in all Zn-Li alloy samples. The lattice parameters were different from the literature and were corrected according to the XRD results (Space Group: *Cmcm*, a=2.818 Å, b=4.812 Å, c=4.363 Å, α = β = γ =90°). The intensity of the α -LiZn₄ peaks increased as Li amount increased, suggesting an increasing amount of this phase. Strong diffraction peaks emerged at low angles (such as in the range of 18.2°~18.5°) and might derive from an unknown LPSO (Long Period Stacking Ordered) phase considering the large d-spacing they represented [31].

Fig. 2 reveals the Inverse Pole Figure (IPF) maps of pure zinc and experimental Zn-Li binary alloys, corresponding microstructure features were summarized in Table 1. Hot extruded pure zinc (Fig. 2a) had near equiaxed grains and an average grain size of 95 \pm 59 μm . It also possessed typical $<01\bar{1}0>-<\bar{1}2\bar{1}0>$ double fiber texture, which was commonly observed in hot extruded h.c.p. metals [32]. Alloying with 0.1wt.%Li significantly refined the grains to 2.7 \pm 1.3 μm (Fig. 2b) and introduced a small fraction (\sim 4%) of new texture whose extrusion direction (ED) was parallel to <0001>. When the lithium amount reached 0.4wt.% (Fig. 2c), the average grain size decreased to 2.0 \pm 0.9 μm and the fraction of the newly formed texture reached 19%.

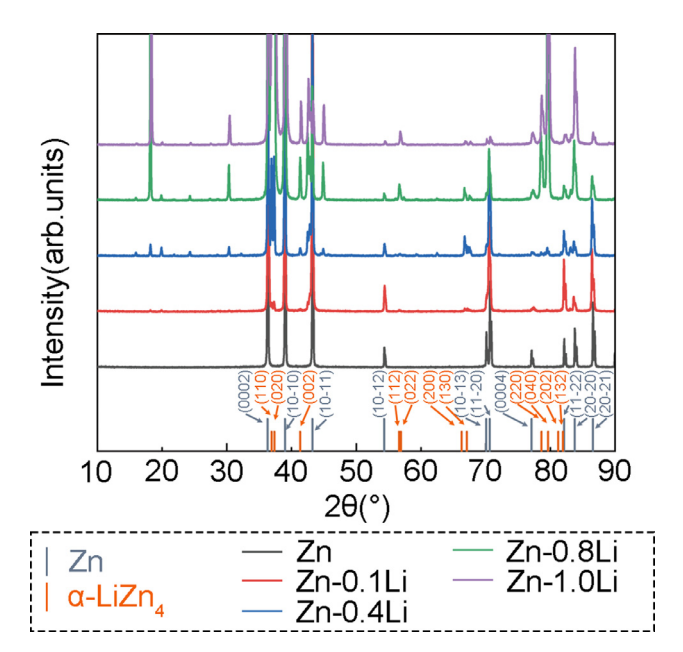


Fig. 1. Phase identification of the studied materials.

Table 1 Microstructure parameters of the investigated materials. (f_{Eu} : Area fraction of the eutectoid region.)

Materials	Grain Size in Equiaxed Grain Regions (μm)	f _{Eu} (%)
Pure zinc	95 ± 59	0
Zn-0.1wt.%Li	2.7 ± 1.3	4
Zn-0.4wt.%Li	2.0 ± 0.9	19
Zn-0.8wt.%Li	2.1 ± 0.8	44
Zn-1.0wt.%Li	-	100

Table 2Monotonic mechanical properties of pure zinc and Zn-Li alloys. (Eu: Uniform Elongation, El: Fracture Elongation.)

Tensile	YS/MPa	UTS/MPa	Eu/%	El/%
Pure zinc	38.9 ± 1.0	106.5 ± 2.4	19 ± 1	22 ± 4
Zn-0.1wt.%Li	319 ± 11	319 ± 11	3.2 ± 0.1	39 ± 2
Zn-0.4wt.%Li	337 ± 14	434 ± 18	4.6 ± 0.1	52 ± 4
Zn-0.8wt.%Li	412.7 ± 0.6	576 ± 6	6.5 ± 0.1	61 ± 11
Zn-1.0wt.%Li	434.2 ± 1.4	661 ± 2	5.4 ± 0.1	52.7 ± 2.1
Compressive	YS/MPa			
Pure zinc	122 ± 3			
Zn-0.1wt.%Li	267 ± 19			
Zn-0.4wt.%Li	432 ± 9			
Zn-0.8wt.%Li	558 ± 6			
Zn-1.0wt.%Li	679 ± 3			

Further increasing the lithium amount to over 0.8wt.% induced a series of complexity. Firstly, the newly formed texture (with ED||<0001>) became prevalent and its fraction boosted to 44%, and 100% respectively for Zn-0.8wt.%Li and Zn-1.0wt.%Li alloy. These regions had a lamellar structure that was probably formed by the eutectoid reaction at 65°C [33]. The remaining portion in Zn-0.8wt.%Li alloy still exhibited the original double fiber texture and an equiaxed structure with an average grain size of 2.1 \pm 0.8 μ m. Hereafter, the two regions with totally different microstructures will be referred to as the eutectoid region and the equiaxed grain region separately. Secondly, although XRD results confirmed the existence of the α -LiZn₄ phase, EBSD analysis recognized only the Zn phase. Current opinions believed that those equiaxed grains and 200nm-thick lamellae with their<0110>||ED should be Zn, while the rest regions with their<0001> ||ED should belong to the α -LiZn₄ phase [34,35]. Finally, grain boundaries in the equiaxed regions were well-defined but became discontinuous in eutectoid regions. The α -LiZn₄ phase and Zn phase inside eutectoid regions showed a misorientation similar to $\{10\overline{1}2\}<10\overline{1}\}>$ deformation twins $(86^{\circ} < 12\overline{10} >)$.

3.2. Monotonic mechanical tests

Fig. 3 gives the tensile (Fig. 3a) and compressive (Fig. 3b) engineering stress-strain curves of pure zinc and Zn-Li binary alloys obtained under room temperature at an initial strain rate of $\dot{\varepsilon}=10^{-3}/s$. Obtained mechanical parameters are listed in Table 2. Under monotonic condition, pure zinc had a tensile yield strength (YS) of 38.9 \pm 1.0MPa and an ultimate tensile strength (UTS) of 106.5 ± 2.4 MPa. It exhibited work hardening after yielding and had a uniform elongation of $19 \pm 1\%$ followed by a sudden fracture without necking. Alloying with Li effectively strengthened the materials. The improved UTS reached 319 ± 11 MPa for Zn-0.1wt.%Li alloy. As the lithium amount increased, the tensile YS and UTS increased simultaneously for Zn-Li binary alloys. The highest value was obtained by Zn-1.0wt.%Li alloy, which gave a YS of 434.2 \pm 1.4MPa and a UTS of 661 ± 2 MPa. However, it was observed that necking became more obvious and the work softening be-

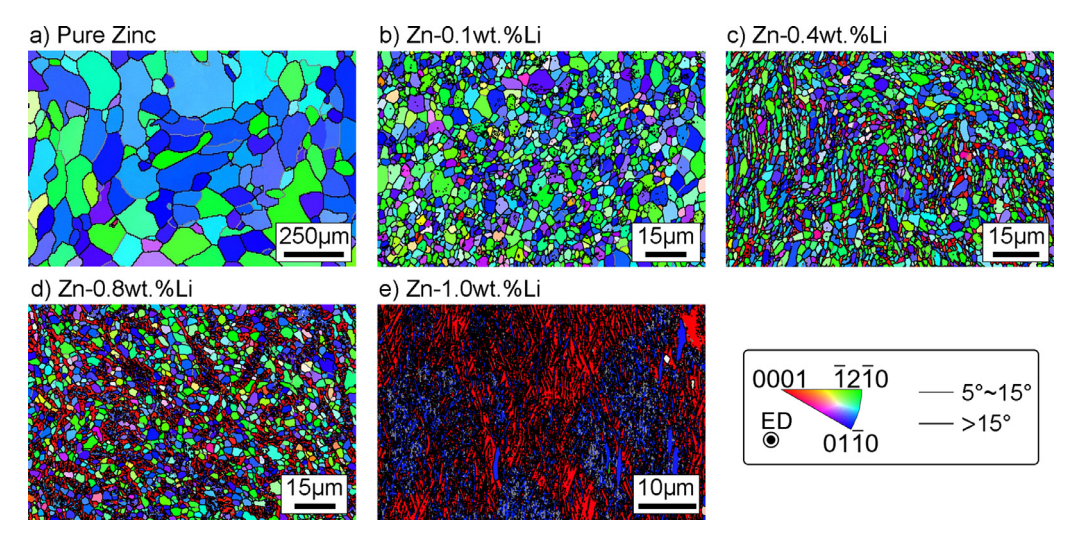


Fig. 2. EBSD analysis of the investigated materials: a) Pure zinc. b) Zn-0.1wt.%Li alloy. c) Zn-0.4wt.%Li alloy. d) Zn-0.8wt.%Li alloy. e) Zn-1.0wt.%Li alloy. (Figures here demonstrate the Inverse Pole Figure maps which reflect the orientation of extrusion direction).

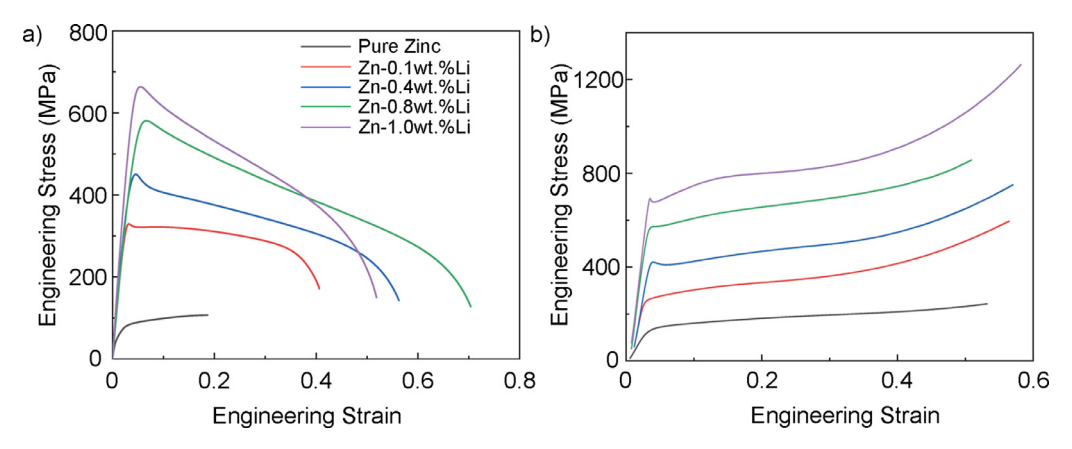


Fig. 3. Stress-Strain curves of pure zinc and Zn-Li alloys under a) Tensile tests. b) Compressive tests.

Table 3Fatigue strength and fatigue limit values of the investigated materials.

Materials	Fatigue Limit (Air)/MPa	Fatigue Strength (Air, 10 ⁷)/MPa	Fatigue Limit (SBF)/MPa	Fatigue Strength (SBF, 10 ⁷)/MPa
Pure Zinc	6.2	20.3	7.1	24.4
Zn-0.1wt.%Li	52.5	73.9	26.8	53.0
Zn-0.4wt.%Li	61.4	89.8	9.2	50.8
Zn-0.8wt.%Li	66.0	98.7	25.5	67.9
Zn-1.0wt.%Li	70.7	117.5	9.7	52.0

havior was more prominent at the same time (the slope became steeper downwards). During compressive tests, all materials kept deforming without failure and the tests were stopped at a strain of about 0.6. Similarly, compressive YS became higher as the lithium amount rose and the highest value reached 679 \pm 3MPa for Zn-1.0wt.%Li alloy. Tension-compression yield asymmetry was significant for all the experimental Zn-Li binary alloys, and the compressive YS was usually higher, as had been reported in another work [36].

3.3. Fatigue and corrosion fatigue tests

Fig. 4 gives the fatigue and corrosion fatigue results. Calculated mechanical parameters were listed in Table 3. In each case, the fa-

tigue strength for a predetermined fatigue life of 10⁷ cycles was calculated using the Basquin model [37]:

$$\sigma = C_1 N^{C2} \tag{1}$$

where σ is the stress amplitude, N is the number of cycles to failure, and C_1 and C_2 are material constants. As can be seen from Fig. 4a and c, the fatigue strength of pure zinc was as low as 20.3MPa in air and slightly increased to 24.4MPa when corrosion was introduced. Generally, fatigue strength increased with monotonic mechanical strength in air and reached a maximum in Zn-1.0wt.%Li alloy (117.5MPa). But in SBF, fatigue strength dropped significantly for Zn-Li binary alloys.

In addition, fatigue limits were calculated based on Stromeyer law [37] (Fig. 4b and d):

$$\sigma = \sigma_{\rm W} + C \left(10^6/N\right)^{1/4} \tag{2}$$

where σ is the stress amplitude, σ_w is the fatigue limit, N is the number of cycles to failure and C is a material constant. Pure zinc had a fatigue limit of 6.2MPa in air, while Zn-1.0wt.%Li alloy had a much higher fatigue limit of 70.7MPa. In a corrosive environment, the fatigue limit value turned out to be slightly higher for pure zinc (7.1MPa) and dropped drastically for Zn-Li binary alloys. Zn-1.0wt.%Li alloy, which possessed the highest fatigue limit in air, had a fatigue limit of only 9.7MPa in SBF.

Fig. S1 presents the hysteresis loops of the 5th to the 5000000th cycle during stress-controlled fatigue tests in air. The shrinking

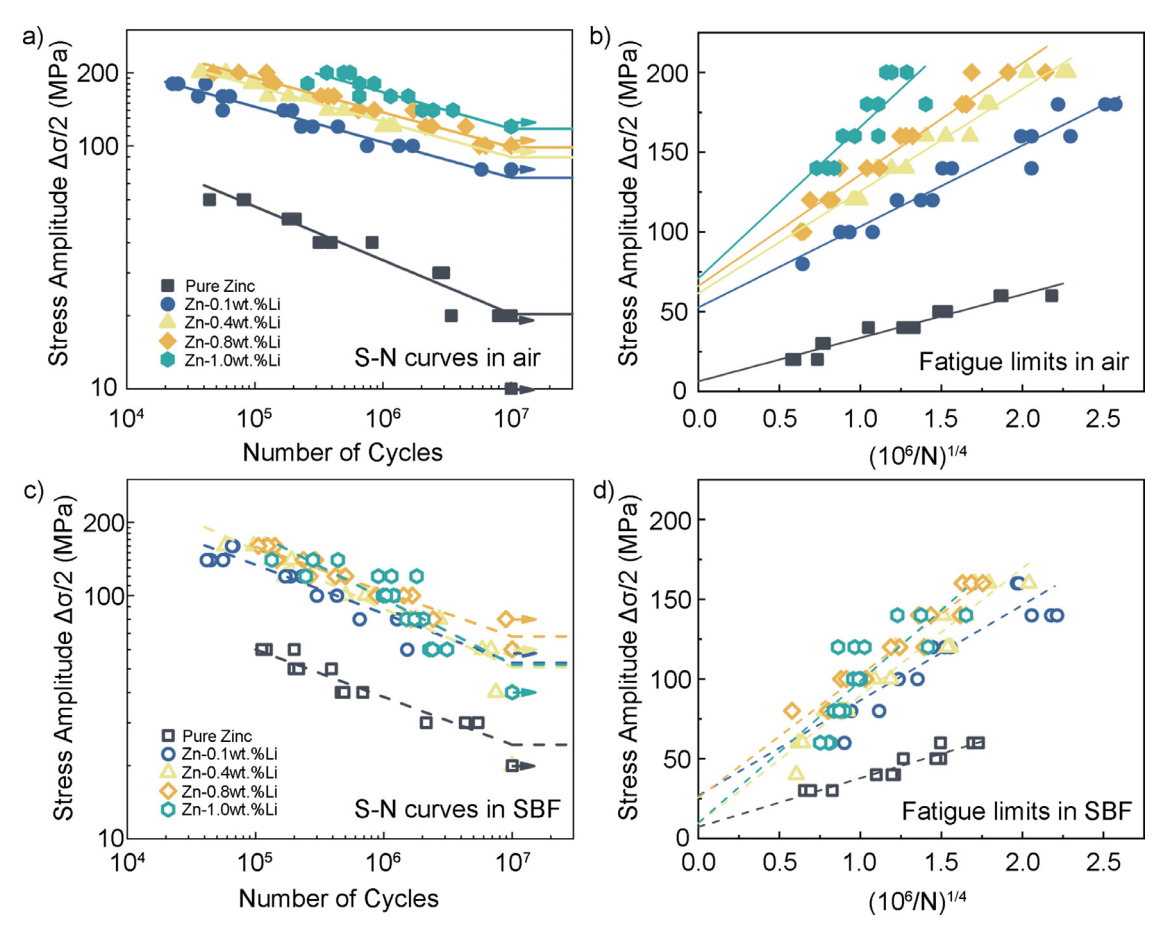


Fig. 4. Fatigue behaviors of the investigated materials in air: a) S-N curves, b) Fatigue limit analysis, and in SBF: c) S-N curves, d) Fatigue limit analysis.

strain amplitude reflected the slight cyclic hardening effect of the four binary alloys. Pure zinc, on the other hand, showed no such hardening since the strain amplitude remained almost unchanged. Fatigue tests in circulating SBF showed similar results and thus were not shown.

3.4. Fatigue fracture analysis and crack morphology

Fig. 5 shows typical high-cycle fatigue fracture surfaces produced in air. For each kind of metal, an overview of the fracture surface, a magnified view of the crack propagation zone, and a magnified view of the overload zone were given in series. In the overview, the crack initiation site, the propagation zone, and the overload zone were separated using yellow and red dashed lines, respectively. Meanwhile, the direction of crack propagation was indicated using orange arrows. It was obvious that the fracture surface of pure zinc (Fig. 5a) was rough, while for Zn-Li alloys (Fig. 5bd) the fracture surfaces were rather flat. A large portion of the fracture surfaces belonged to the crack propagation zone. White arrows pointed out the locations of typical fatigue striations which were characteristic lines formed due to partially reversed slip at crack tips [38]. These striations were observed on cleavage surfaces that were considered to locate in equiaxed grain regions. When cracks propagated through the eutectoid regions, quasi-cleavage fracture occurred and flutes were formed as indicated by the black arrows. High magnification images for striations and flutes were provided in Fig. S6. When an active crack grew to a critical size, fracture occurred similarly to monotonic overloading, and fractography resembled tensile fracture surfaces in the overload zone.

Fig. 6 presents the fracture surfaces of samples after corrosion fatigue in SBF. Corrosion products were cleaned in hot chromic acid. Compared with those in Fig. 5, fracture surfaces became rougher for samples undergoing corrosion fatigue. Generally, more than one crack initiation site could be found and overload zones stood in the middle of the samples. The middle column in Fig. 6 shows the magnified view of crack initiation sites, and white arrows pointed out the corrosion pits. These localized corrosion events could be one of the drives for crack propagation. Flutes were observed only on pure zinc (black arrows) and might be covered by the corrosion attack in Zn-Li alloys. Deep secondary cracks that were rarely seen in Fig. 5 were very common in the overload zones of corrosion-fatigued samples, especially those with high lithium content (Fig. 6d-e).

For a better interpretation of the crack propagation and the influence of corrosion, failed samples were mounted and cut along the loading direction to reveal the crack morphology inside. Fig. 7 shows the results for Zn-0.1wt.%Li alloy. Pure zinc and Zn-0.4wt.%Li alloy showed a similar pattern and their results are presented in Fig. S2-3. Generally, fatigue crack propagation in these materials was not significantly intensified by corrosion. For pure zinc (Fig. S2), although fracture surfaces were rough, secondary cracks turned out to be shallow for both testing conditions. Most of them were about 20 µm long and very few of them exceeded 100 µm (Region A, Fig. S2g). Zn-0.1wt.%Li and Zn-0.4wt.%Li alloys showed similar results (Fig. 7, S3), with slightly extended secondary cracks observed in Zn-0.4wt.%Li alloy. However, for Zn-0.8wt.%Li and Zn-1.0wt.%Li alloys, the drastic effect of corrosion on crack propagation was captured. Fig. S4 and Fig. S5 compare the cracks observed in Zn-0.8wt.%Li alloy under different fatigue conditions. When tested

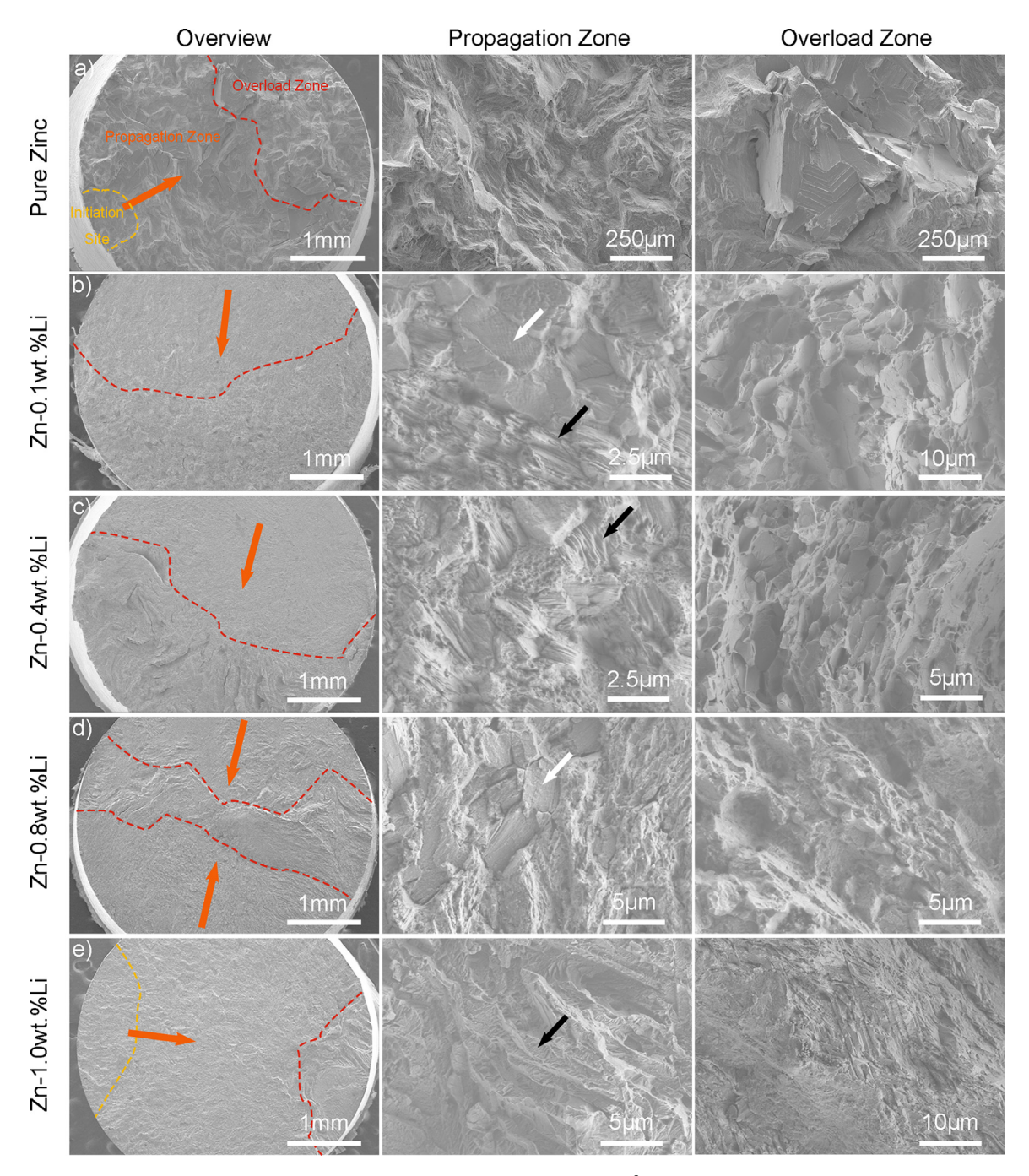


Fig. 5. Fracture surface images of samples fatigued in the air: a) Pure zinc, $\Delta\sigma/2=20$ MPa, N=3.4 × 10⁶ cycles. b) Zn-0.1wt.%Li alloy, $\Delta\sigma/2=100$ MPa, N=1.3 × 10⁶ cycles. c) Zn-0.4wt.%Li alloy, $\Delta\sigma/2=120$ MPa, N=1.1 × 10⁶ cycles. d) Zn-0.8wt.%Li alloy, $\Delta\sigma/2=120$ MPa, N=2.1 × 10⁶ cycles. e) Zn-1.0wt.%Li alloy, $\Delta\sigma/2=140$ MPa, N=2.0 × 10⁶ cycles. (Yellow and red lines denote the location of crack initiation sites and overload zones separately, while the orange arrows point out the crack propagating directions. White and black arrows point to the observed fatigue striations and flutes, respectively.)

in the air (Fig. S4), very few secondary cracks could be observed, but when tested in SBF (Fig. S5), long cracks of over 100 μm long extended from the fracture surface. The propagation of such cracks is parallel to the loading direction and thus should be driven mainly by corrosion instead of cyclic stress. An even more significant effect of corrosion was observed in Zn-1.0wt.%Li alloy (Figs. 8, 9), where secondary cracks were extended from $\sim\!\!20~\mu m$ in the air to over 250 μm in SBF. The adverse effect of intensely extended crack propagation lay in that multiple cracks could be connected, undermining the loading capacity of the material. The abovementioned phenomena were summarized in Table 4.

4. Discussion

4.1. Microstructure in fatigued samples

Fig. 10 shows the microstructure of a pure zinc sample after cyclic loading. Chains of recrystallized grains that were aligned perpendicular to the loading direction were formed in a large parent grain. A few discontinuous low-angle grain boundaries were observed and a very low dislocation density was presented throughout the whole region. The location of recrystallized grains might demonstrate sites where deformation was concentrated, as had

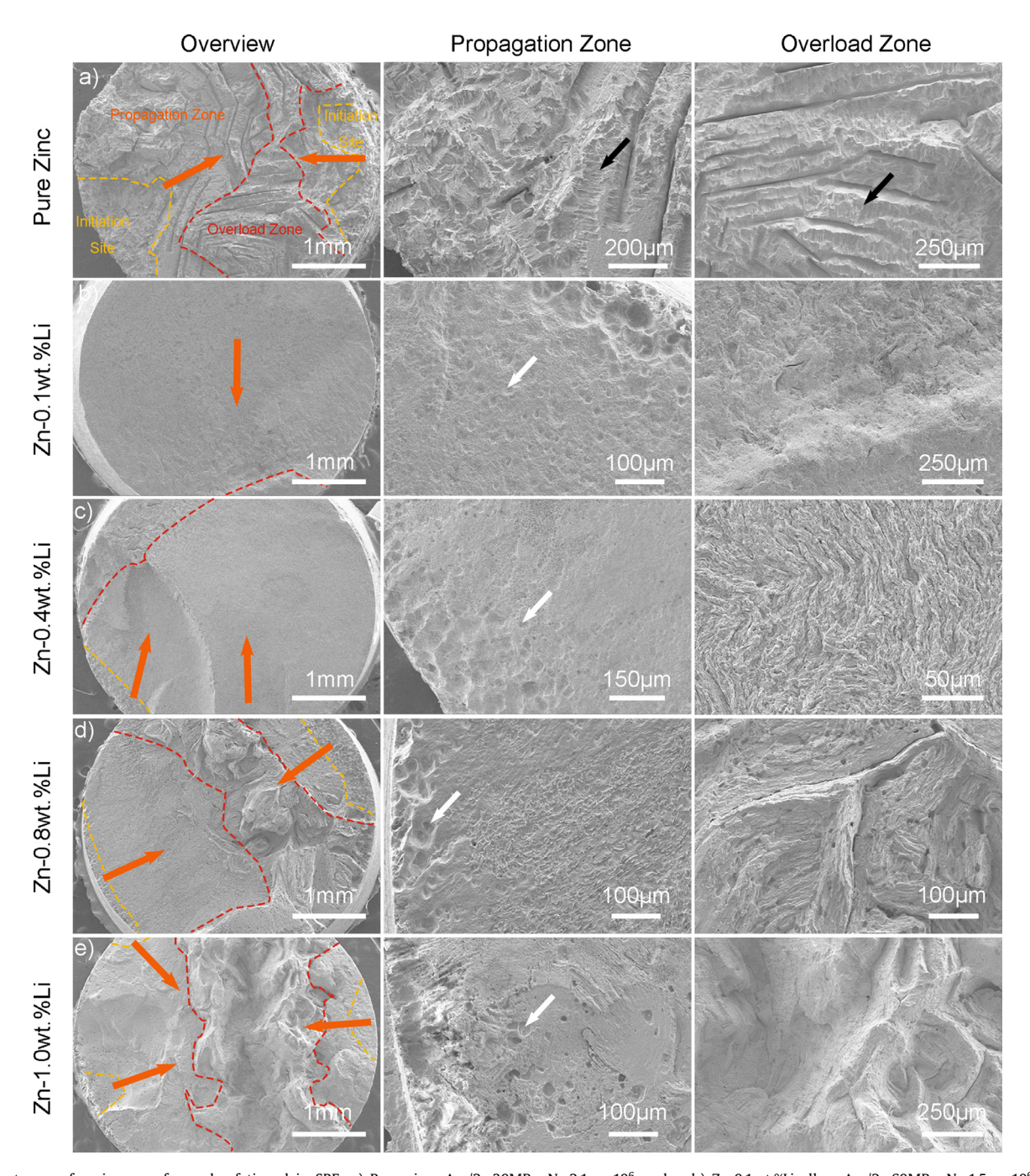


Fig. 6. Fracture surface images of samples fatigued in SBF: a) Pure zinc, $\Delta\sigma/2=30$ MPa, $N=2.1\times10^6$ cycles. b) Zn-0.1wt.%Li alloy, $\Delta\sigma/2=60$ MPa, $N=1.5\times10^6$ cycles. c) Zn-0.4wt.%Li alloy, $\Delta\sigma/2=40$ MPa, $N=7.5\times10^6$ cycles. d) Zn-0.8wt.%Li alloy, $\Delta\sigma/2=80$ MPa, $N=1.6\times10^6$ cycles. e) Zn-1.0wt.%Li alloy, $\Delta\sigma/2=60$ MPa, $N=2.3\times10^6$ cycles. (Yellow and red lines denote the location of crack initiation sites and overload zones separately, while the orange arrows point out the crack propagating directions. White and black arrows point to the observed corrosion pits and flutes, respectively.)

Table 4Observed fatigue crack morphology correlated to material microstructure.

Materials	Microstructure features	Corrosion fatigue crack morphology
Pure zinc	Coarse equiaxed grains	Similar to that of fatigue cracks in air
Zn-0.1wt.%Li and Zn-0.4wt.%Li	Large fraction of equiaxed grain regions mixed with limited eutectoid regions	Similar to that of fatigue cracks in air
Zn-0.8wt.%Li and Zn-1.0wt.%Li	Large fraction of eutectoid regions	Significantly extended in length compared to fatigue cracks in air

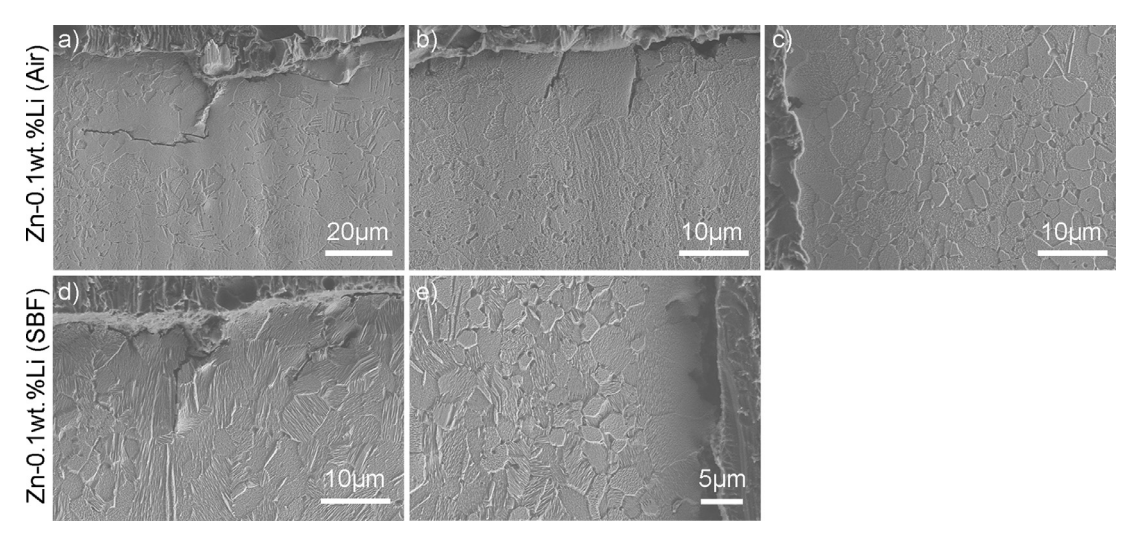


Fig. 7. Secondary crack and microcrack morphology on longitudinal sections of Zn-0.1wt.%Li specimens: a-c) A specimen tested in air, $\Delta \sigma/2$ =80MPa, N=5.8 × 10⁶ cycles. d-e) A specimen tested in SBF, $\Delta \sigma/2$ =60MPa, N=1.5 × 10⁶ cycles.

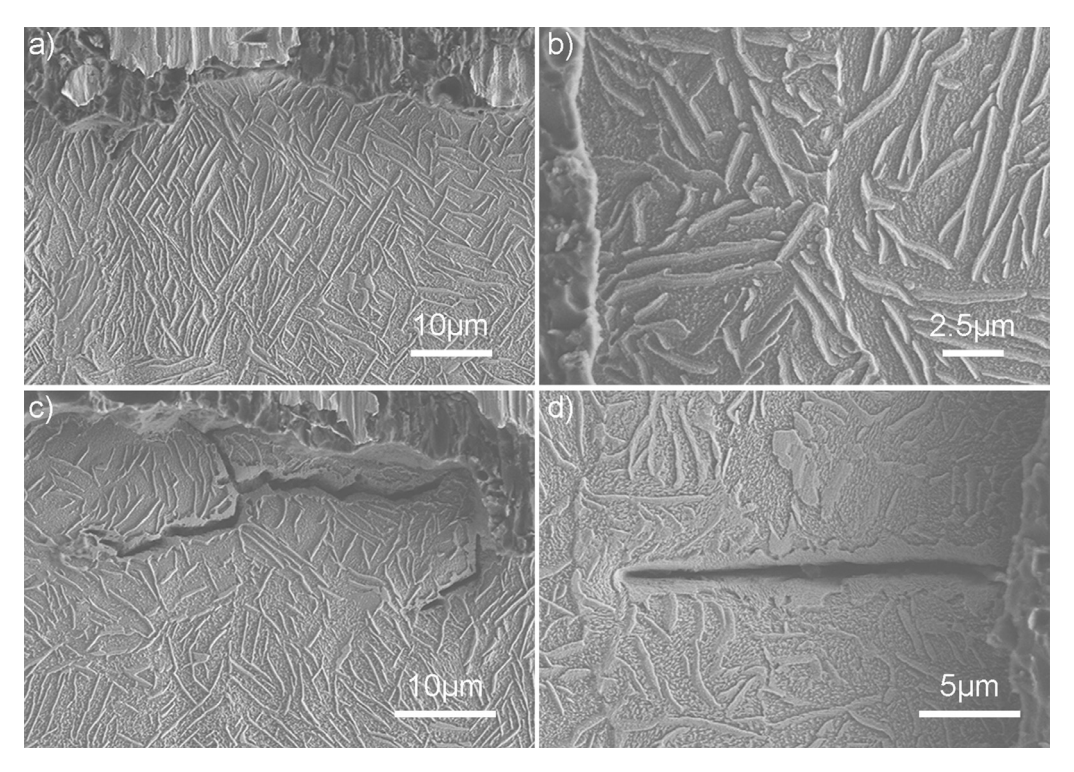


Fig. 8. Secondary and microcrack morphology on the longitudinal section of a Zn-1.0wt.%Li specimen tested in air, $\Delta\sigma/2=140$ MPa, N=2.0 \times 10⁶ cycles.

been observed by Li et al. [28]. Meanwhile, some deformation twins were triggered and might participate in the dynamic recrystallization process. Recrystallization consumed the stored energy in dislocations and explained the absence of work hardening in pure zinc during fatigue.

Persistent slip bands (PSBs) characterized by a ladder-like structure are usually formed in samples after fatigue [15]. These structures denote preferential sites for cyclic deformation and are responsible for cyclic hardening. Fig. S1 has shown that almost no cyclic hardening was observed for pure zinc and very limited cyclic hardening was observed for Zn-Li alloys. This indicated that the cyclic response might vary with microstructure. Fig. 11 presents

the TEM bright field images of a Zn-0.8wt.%Li specimen fatigued in air. Large differences in dislocation density and structure were found in different regions. In eutectoid regions, dislocation vein structures and sparse PSBs could be found, indicating a high dislocation density (Fig. 11a). In contrast, very few dislocations were observed in equiaxed grain regions (Fig. 11b). The boundaries between the two regions also appeared as boundaries that separated regions with different dislocation densities (Fig. 11c-d). Such results suggested a disparity in dislocation storing ability between the two regions and further explained the enhanced fatigue strength in Zn-Li alloys with a large fraction of eutectoid regions.

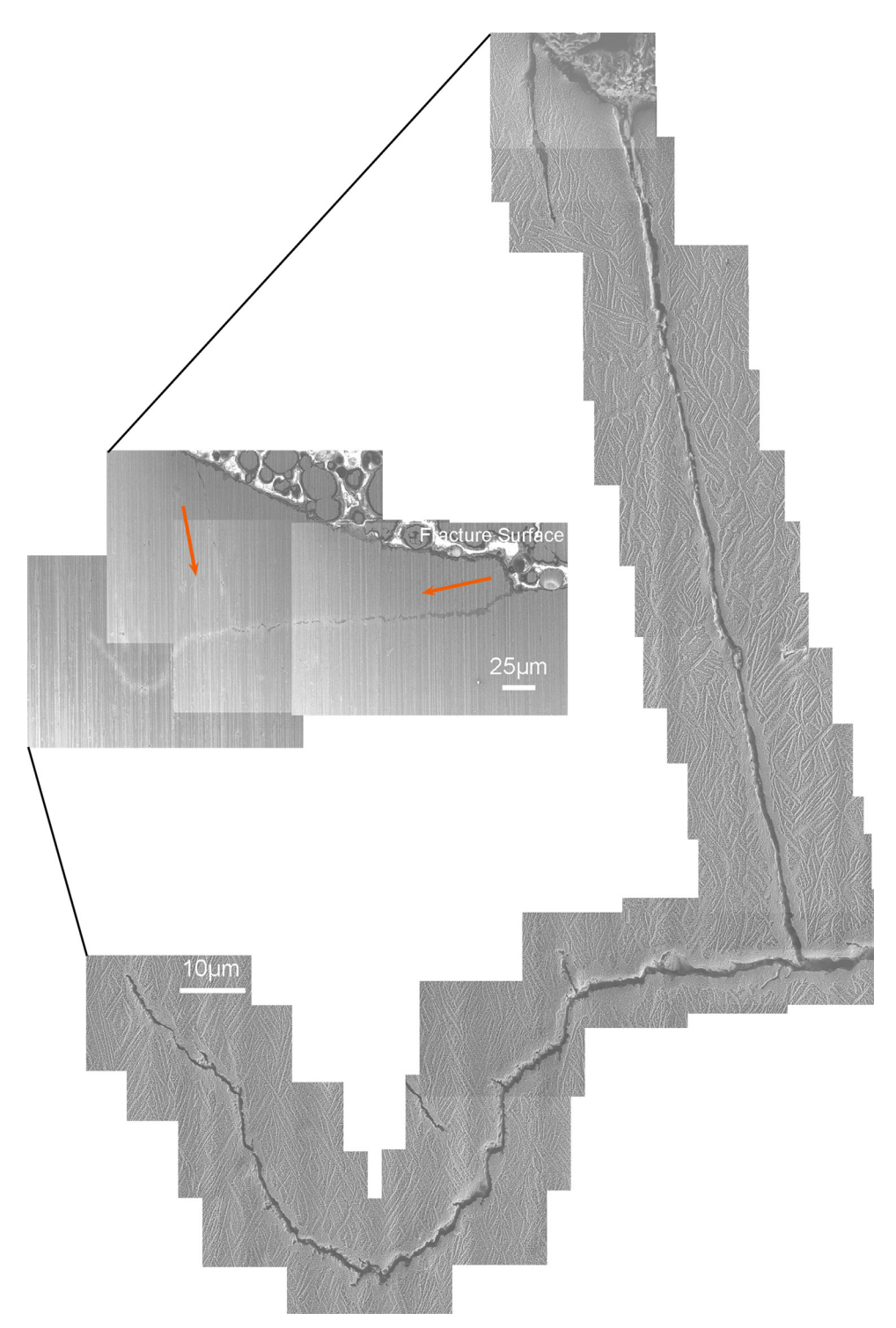


Fig. 9. Secondary crack morphology on the longitudinal section of a Zn-1.0wt.%Li specimen tested in SBF, $\Delta\sigma/2$ =60MPa, N=2.3 \times 10⁶ cycles. (Orange arrows denote the crack propagating directions of two secondary cracks that intersected. Note that the length of secondary cracks was extremely extended compared to Fig. 8).

4.2. Fatigue crack propagation in corrosive environments

Fig. 12a-c presents the microstructure near a crack tip in pure zinc fatigued in SBF. This crack lay perpendicular to the loading direction (Fig. 12c). Apparently, the crack propagated in an intergranular manner which could be related to the localized corrosion at grain boundaries [39]. However, very few branches were observed and the preferential dissolution at grain boundaries was

therefore believed to be mild. This was supported by the similarity in secondary crack lengths between samples fatigued in air and SBF (Fig. 9).

Fig. 12d-e gives the EBSD results near a crack tip in Zn-0.4wt.%Li alloy. The sample fractured in SBF after millions of cycles, and the captured crack tip propagated entirely in the equiaxed grain region. In Zn-0.4wt.%Li alloys, fatigue cracks were usually short and lay perpendicular to the loading direction. The prop-

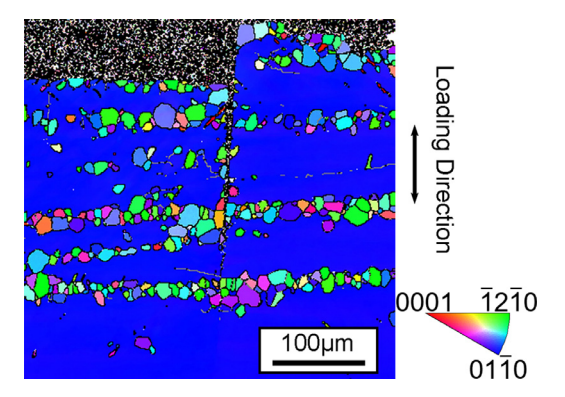


Fig. 10. Microstructure of pure zinc near fatigue fracture.

agation of such cracks was driven by both corrosion and cyclic stress. By comparing the band contrast map (Fig. 12e) and the IPF map (Fig. 12d), it could be concluded that both intergranular and transgranular fractures took place. Red crossings denoted sites where transgranular fractures occurred. This suggested the lack of a predominant fracture mode in these equiaxed grain regions.

Li et al. showed that in additively manufatured porous pure zinc, fatigue cracks propagated dominantly in a transgranular manner both in air and in SBF [28]. Besides, dynamic recovery and recrystallization were observed around crack tips. Fegredo et al. came up with the opposite conclusion that fatigue cracks propagated predominantly by intergranular fracture [26]. According to our observation, in the equiaxed grain regions of Zn-Li alloys, fatigue cracks propagated in a mixed mode.

Strongly intensified crack propagation could be attributed to high lithium content, which also represented a large area fraction of eutectoid regions. Fig. 12f illustrates the EBSD analysis around a crack tip in Zn-1.0wt.%Li alloy which was composed purely of eutectoid structures. It was believed that the Zn and α -LiZn₄ phases distributed in an intertwined manner, and thus lack of the α -LiZn₄ phase around the captured crack suggested preferential dissolution of this phase during crack propagation. This phenomenon should not be surprising considering the much higher lithium amount in this phase, as had been demonstrated via direct or indirect methods [10,34,40]. With the help of this new driving force, corrosion fatigue cracks proceeded more easily in Zn-0.8wt.%Li and Zn-1.0wt,%Li alloys. This mode of crack propagation could be terminated by equiaxed grain regions where preferential dissolution no longer existed. However, in Zn-1.0wt.%Li alloy where no equiaxed grain region stood, cracks propagated freely throughout the whole material till fracture. This could explain the significantly undermined corrosion fatigue strength of the Zn-1.0wt.%Li alloy observed.

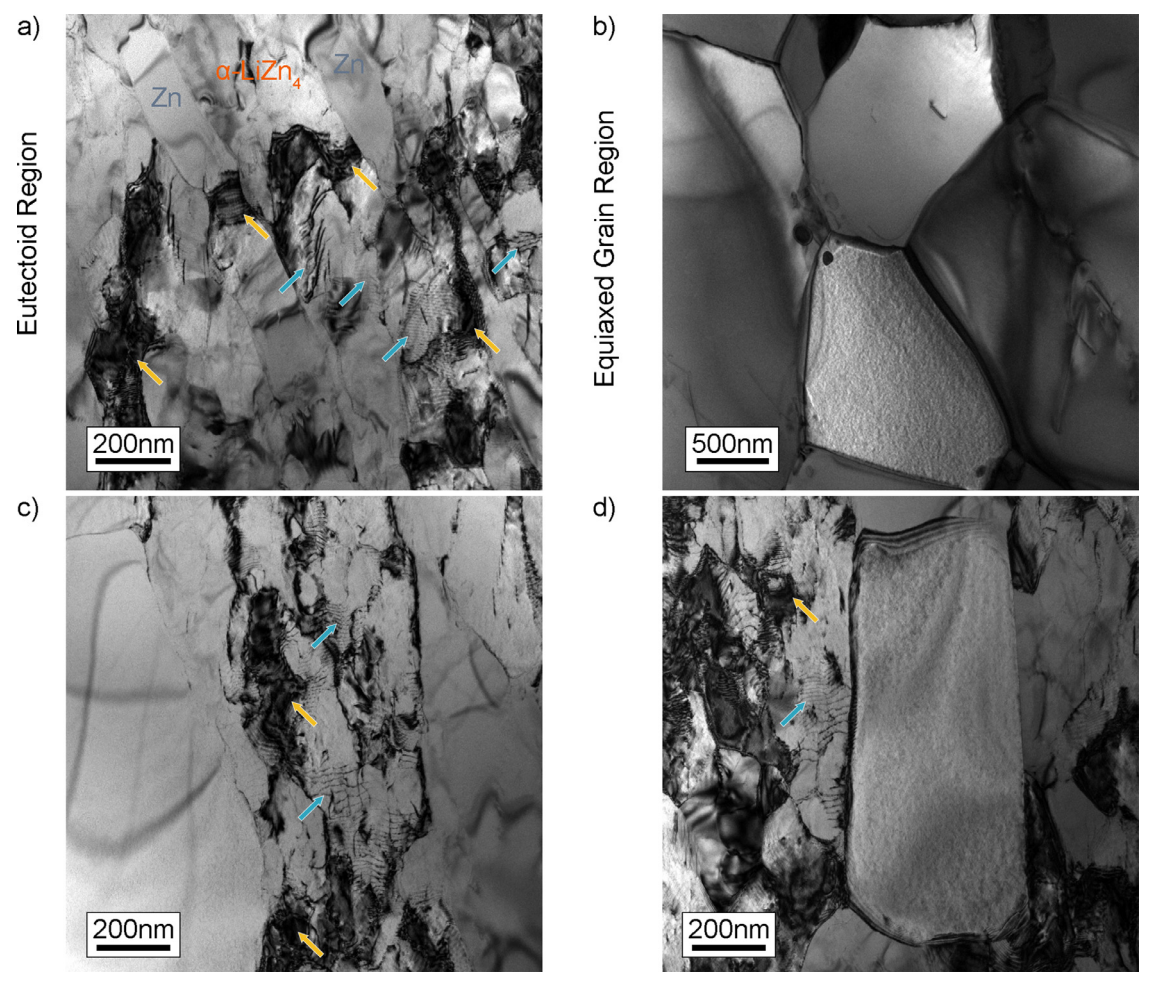


Fig. 11. Microstructure near fatigue fracture of a Zn-0.8wt.%Li specimen: a) Dislocation structure in eutectoid regions. b) Microstructure of equiaxed grain regions. c-d) Microstructure of eutectoid regions and equiaxed grain regions in the same view. Note the great difference in dislocation density. (Grey and orange texts marked Zn lamellae and the nearby α -LiZn₄ phase. Yellow and blue arrows point to dislocation vein structures and PSBs respectively).

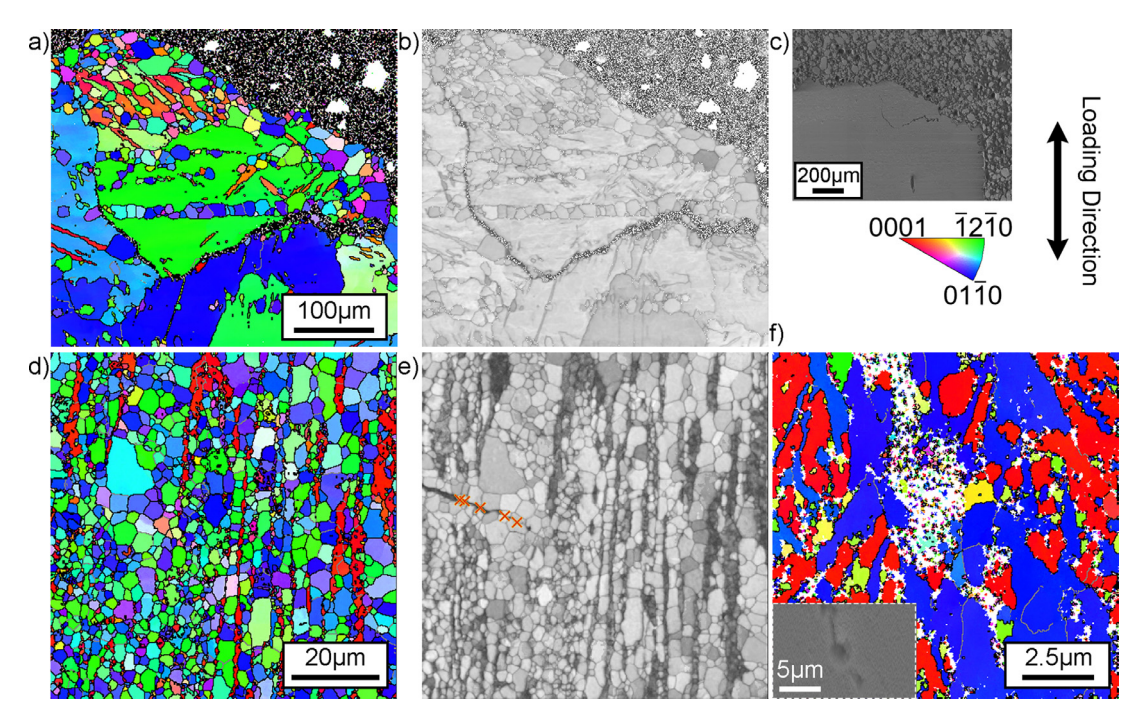


Fig. 12. Crack propagation during corrosion fatigue. a-c) Pure zinc: a) IPF map around the crack, b) Band contrast map at the same site, c) Macroscopic view of the investigated crack. d-e) Zn-0.4wt.%Li alloy: d) IPF map around the crack tip, e) Band contrast map at the same site. (Red crossings mark the sites where transgranular fractures occur.) f) Zn-1.0wt.%Li alloy: f) IPF map around the crack tip. (Inset shows the macroscopic view.).

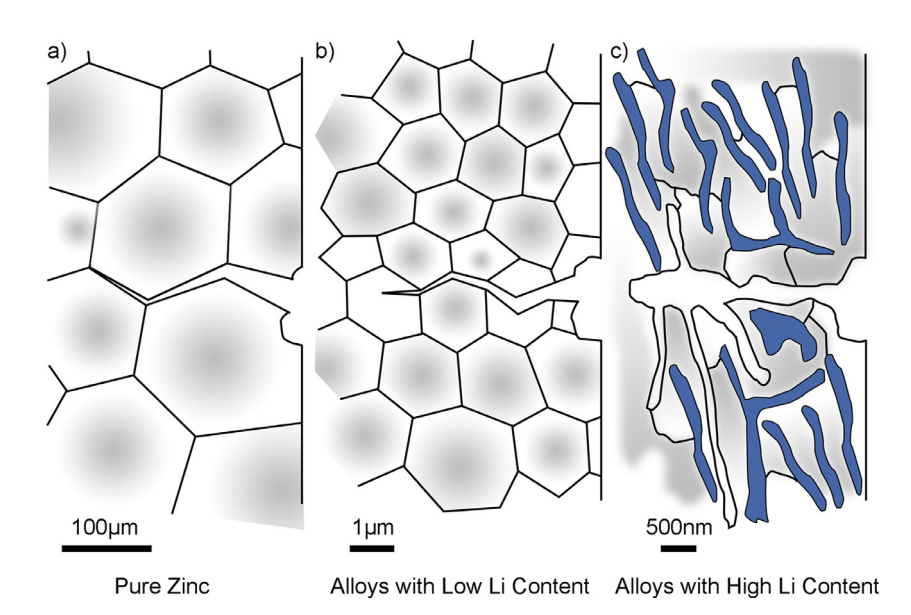


Fig. 13. Schematic diagram illustrating the mechanisms of corrosion fatigue crack propagation in different materials: a) Pure zinc. b) Alloys with low lithium content (Zn-0.1wt.%Li and Zn-0.4wt.%Li alloys) and composed mainly of equiaxed grain structures. c) Alloys with high lithium content with a large fraction of eutectoid regions (Zn-0.8wt.%Li and Zn-1.0wt.%Li alloys).

Fig. 13 depicts the proposed mechanisms for fatigue crack propagation under corrosive conditions. For pure zinc, cracks propagated in an intergranular manner, which was attributed to localized corrosion at grain boundaries. In Zn-Li alloys with low lithium content i.e., Zn-0.1wt.%Li and Zn-0.4wt.%Li alloys, the microstructure was predominantly equiaxed grain structure. Fatigue cracks propagated in a mixed manner with no preferential propagation path due to chemical homogeneity. On the contrary, in Zn-0.8wt.%Li and Zn-1.0wt.%Li alloys, eutectoid regions accounted for a large portion of the microstructure and cracks propagated by selec-

tive dissolution of the $\alpha\text{-LiZn}_4$ phase, which led to enhanced secondary crack growth.

4.3. Fatigue strength comparison with other biodegradable alloys and pure titanium

Zn-Li alloys are promising candidates for a new generation of biodegradable metals largely due to their outstanding mechanical properties that are comparable to pure titanium [6,9,11]. As shown in Fig. 14a, the present study proved that they possessed com-

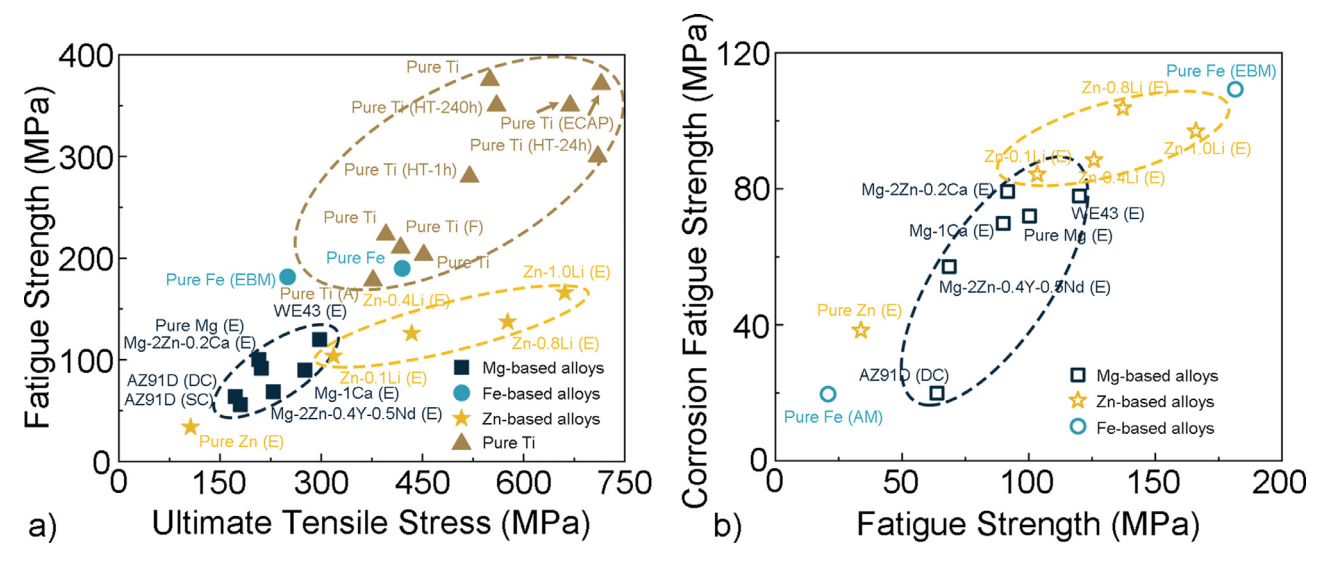


Fig. 14. Comparison of fatigue behaviors between Mg-based, Fe-based, Zn-based alloys, and pure titanium: a) Fatigue strength-UTS. b) Corrosion fatigue strength-fatigue strength [20-22,41-46]. (A: Annealed, E: Extruded, AM: Additively Manufactured, HT: Heat Treated, SC: Sand Casted, DC: Die Casted, EBM: Electron Beam Melted, ECAP: Equal Channel Angular Pressed).

petitive fatigue strength, which was slightly lower than pure iron and pure titanium but higher than magnesium alloys [20-22,41-46]. As regards corrosion fatigue property (Fig. 14b), Zn-Li alloys outperformed Mg-based alloys and remained comparable to pure iron. Copper addition could further improve their corrosion fatigue strength [29]. This further elucidated that Zn-Li alloys could maintain sufficient mechanical integrity in a rather long time range.

5. Conclusions

In this research, fatigue and corrosion fatigue behavior of biodegradable Zn-Li binary alloys were studied with pure zinc as a control. Microstructure analysis was conducted to help clarify the underlying mechanisms of crack propagation. The main conclusions were as follows:

Lithium addition led to the formation of eutectoid regions in Zn-Li alloys and strengthened the materials without ductility sacrifice. Monotonic mechanical strength reached its maximum when 1.0wt.% lithium was introduced and a microstructure with pure eutectoid structure was formed.

Fatigue strength rose synchronously with lithium content and monotonic strength, however, corrosion fatigue strength was adversely affected when lithium content reached 1.0wt.%. Zn-1.0wt.%Li alloy owned the highest fatigue strength of 117.5MPa and Zn-0.8wt.%Li alloy exhibited the highest corrosion fatigue strength of 67.9MPa.

Massive dynamic recrystallization was triggered in pure zinc during cyclic loading, which explained the absence of work hardening. Equiaxed grain regions in Zn-Li alloys behaved similarly where few dislocations were captured. In contrast, dislocation vein structures and sparse PSBs were observed in eutectoid regions which accounted for the observed work hardening during cyclic loading.

Cracks found a new way of propagation in Zn-0.8wt.%Li and Zn-1.0wt.%Li alloys. This was based on chemical heterogeneity and preferential dissolution of the α -LiZn₄ phase in eutectoid regions. Notably longer cracks were formed in such manner. Therefore, the corrosion fatigue strength was significantly lowered for Zn-1.0wt.%Li alloy.

Fatigue strength comparable to pure iron and pure titanium was attained by extruded Zn-Li alloys. This further guaranteed

the mechanical integrity necessary for tissue regeneration after implantation.

Declaration of Competing Interest

The authors declare that they have no known competing financial interests or personal relationships that could have appeared to influence the work reported in this paper.

Acknowledgements

This work was supported by Beijing Natural Science Foundation (Grant No. L212014), National Natural Science Foundation of China (Grant Nos. 51931001 and U22A20121), Fund for International Cooperation and Exchange between NSFC (China) and CNR (Italy) (NSFC-CNR Grant No. 52011530392), Fund for International Cooperation and Exchange between NSFC (China) and RFBR (Russia) (NSFC-RFBR Grant No. 52111530042), and the Open Project of NMPA Key Laboratory for Dental Materials (Grant No. PKUSS20200401).

Supplementary materials

Supplementary material associated with this article can be found, in the online version, at doi:10.1016/j.actbio.2023.07.030.

References

- [1] Y.F. Zheng, X.N. Gu, F. Witte, Biodegradable metals, Mater. Sci. Eng. R 77 (2014) 1–34
- [2] Y. Liu, Y. Zheng, X.H. Chen, J.A. Yang, H. Pan, D. Chen, L. Wang, J. Zhang, D. Zhu, S. Wu, K.W.K. Yeung, R.C. Zeng, Y. Han, S. Guan, Fundamental theory of biodegradable metals—definition, criteria, and design, Adv. Funct. Mater. 29 (18) (2019) 1805402.
- [3] Z. Jia, X. Xu, D. Zhu, Y. Zheng, Design, printing, and engineering of regenerative biomaterials for personalized bone healthcare, Prog. Mater. Sci. 134 (2023) 101072.
- [4] P.K. Bowen, J. Drelich, J. Goldman, Zinc exhibits ideal physiological corrosion behavior for bioabsorbable stents, Adv. Mater. 25 (18) (2013) 2577–2582.
- [5] H. Yang, C. Wang, C. Liu, H. Chen, Y. Wu, J. Han, Z. Jia, W. Lin, D. Zhang, W. Li, W. Yuan, H. Guo, H. Li, G. Yang, D. Kong, D. Zhu, K. Takashima, L. Ruan, J. Nie, X. Li, Y. Zheng, Evolution of the degradation mechanism of pure zinc stent in the one-year study of rabbit abdominal aorta model, Biomaterials 145 (2017) 92–105.
- [6] H. Yang, B. Jia, Z. Zhang, X. Qu, G. Li, W. Lin, D. Zhu, K. Dai, Y. Zheng, Alloying design of biodegradable zinc as promising bone implants for load-bearing applications, Nat. Commun. 11 (1) (2020) 401.

- [7] Y. Zheng, X. Liu, D. Shen, W. Li, Y. Cheng, M. Yang, Y. Kou, B. Jiang, Perceiving the connection between the bone healing process and biodegradation of biodegradable metal implants through precise bioadaptability principle, J. Mater. Sci. Technol. 147 (2023) 132–144.
- [8] D. Xia, Y. Qin, H. Guo, P. Wen, H. Lin, M. Voshage, J.H. Schleifenbaum, Y. Cheng, Y. Zheng, Additively manufactured pure zinc porous scaffolds for critical-sized bone defects of rabbit femur, Bioact. Mater. 19 (2023) 12–23.
- [9] S. Zhao, C.T. McNamara, P.K. Bowen, N. Verhun, J.P. Braykovich, J. Goldman, J.W. Drelich, Structural characteristics and in vitro biodegradation of a novel Zn-Li alloy prepared by induction melting and hot rolling, Metallurg. Mater. Trans. A 48 (3) (2017) 1204–1215.
- [10] Z. Li, Z. Shi, Y. Hao, H. Li, X. Liu, A.A. Volinsky, H. Zhang, L. Wang, High-performance hot-warm rolled Zn-0.8Li alloy with nano-sized metastable precipitates and sub-micron grains for biodegradable stents, J. Mater. Sci. Technol. 35 (11) (2019) 2618–2624.
- [11] Z. Li, Z. Shi, Y. Hao, H. Li, H. Zhang, X. Liu, L. Wang, Insight into role and mechanism of Li on the key aspects of biodegradable Zn-Li alloys: Microstructure evolution, mechanical properties, corrosion behavior and cytotoxicity, Mater. Sci. Eng. C 114 (2020) 111049.
- [12] H. Yang, D. Jin, J. Rao, J. Shi, G. Li, C. Wang, K. Yan, J. Bai, G. Bao, M. Yin, Y. Zheng, Lithium-induced optimization mechanism for an ultrathin-strut biodegradable Zn-based vascular scaffold, Adv. Mater. (2023) 2301074.
- [13] B. Jia, Z. Zhang, Y. Zhuang, H. Yang, Y. Han, Q. Wu, X. Jia, Y. Yin, X. Qu, Y. Zheng, High-strength biodegradable zinc alloy implants with antibacterial and osteogenic properties for the treatment of MRSA-induced rat osteomyelitis, Biomaterials 287 (2022) 121663.
- [14] Z. Zhang, B. Jia, H. Yang, Y. Han, Q. Wu, K. Dai, Y. Zheng, Zn0.8Li0.1Sr-a biodegradable metal with high mechanical strength comparable to pure Ti for the treatment of osteoporotic bone fractures: In vitro and in vivo studies, Biomaterials 275 (2021) 120905.
- [15] S. Suresh, Fatigue of Materials, Cambridge university press, 1998.
- [16] R. Narayan, ASM Handbook, Volume 23, Materials for Medical Devices, 2012.
- [17] R.A. Antunes, M.C.L. de Oliveira, Corrosion fatigue of biomedical metallic alloys: mechanisms and mitigation, Acta Biomater. 8 (3) (2012) 937–962.
- [18] M.A. Meyers, K.K. Chawla, Mechanical Behavior of Materials, Cambridge University Press, 2009.
- [19] M. Niinomi, Fatigue characteristics of metallic biomaterials, Int. J. Fatigue 29 (6) (2007) 992–1000.
- [20] X.N. Gu, W.R. Zhou, Y.F. Zheng, Y. Cheng, S.C. Wei, S.P. Zhong, T.F. Xi, L.J. Chen, Corrosion fatigue behaviors of two biomedical Mg alloys – AZ91D and WE43 – In simulated body fluid, Acta Biomater. 6 (12) (2010) 4605–4613.
- [21] S. Jafari, R.K. Singh Raman, C.H.J. Davies, Corrosion fatigue of a magnesium alloy in modified simulated body fluid, Eng. Fract. Mech. 137 (2015) 2–11.
- [22] D. Bian, W. Zhou, Y. Liu, N. Li, Y. Zheng, Z. Sun, Fatigue behaviors of HP-Mg, Mg-Ca and Mg-Zn-Ca biodegradable metals in air and simulated body fluid, Acta Biomater. 41 (2016) 351–360.
- [23] L. Han, Z. Zhang, J. Dai, X. Li, J. Bai, Z. Huang, C. Guo, F. Xue, C. Chu, The influence of alternating cyclic dynamic loads with different low frequencies on the bio-corrosion behaviors of AZ31B magnesium alloy in vitro, Bioact. Mater. 7 (2022) 263–274.
- [24] Y. Li, K. Lietaert, W. Li, X.Y. Zhang, M.A. Leeflang, J. Zhou, A.A. Zadpoor, Corrosion fatigue behavior of additively manufactured biodegradable porous iron, Corros. Sci. 156 (2019) 106–116.
- [25] D.M. Fegredo, S/N curve variations of polycrystalline zinc due to temperature and grain size, Metall. Mater. Trans. B 3 (7) (1972) 1943–1949.
- [26] D.M. Fegredo, Metallographic observations on polycrystalline zinc fatigued at various temperatures, Can. Metall. Q. 11 (3) (1972) 515–534.

- [27] T. Tanaka, M. Kohzu, Y. Takigawa, K. Higashi, Low cycle fatigue behavior of Zn-22mass%Al alloy exhibiting high-strain-rate superplasticity at room temperature, Scr. Mater. 52 (3) (2005) 231–236.
- [28] Y. Li, W. Li, F.S.L. Bobbert, K. Lietaert, J.H. Dong, M.A. Leeflang, J. Zhou, A.A. Zad-poor, Corrosion fatigue behavior of additively manufactured biodegradable porous zinc, Acta Biomater 106 (2020) 439–449.
- [29] H. Li, Y. Huang, X. Ji, C. Wen, L. Wang, Fatigue and corrosion fatigue behaviors of biodegradable Zn-Li and Zn-Cu-Li under physiological conditions, J. Mater. Sci. Technol. 131 (2022) 48–59.
- [30] V. Pavlyuk, I. Chumak, L. Akselrud, S. Lidin, H. Ehrenberg, LiZn(4 -x) (x = 0.825) as a (3 + 1)-dimensional modulated derivative of hexagonal close packing, Acta Crystallogr. Sect. B 70 (Pt 2) (2014) 212–217.
- [31] C. Liu, Y. Zhu, Q. Luo, B. Liu, Q. Gu, Q. Li, A 12R long-period stacking-ordered structure in a Mg-Ni-Y alloy, J. Mater. Sci. Technol. 34 (12) (2018) 2235–2239.
 [32] M.G. Jiang, C. Xu, H. Yan, G.H. Fan, T. Nakata, C.S. Lao, R.S. Chen, S. Kamado,
- [32] M.G. Jiang, C. Xu, H. Yan, G.H. Fan, T. Nakata, C.S. Lao, R.S. Chen, S. Kamado, E.H. Han, B.H. Lu, Unveiling the formation of basal texture variations based on twinning and dynamic recrystallization in AZ31 magnesium alloy during extrusion, Acta Mater. 157 (2018) 53–71.
- [33] A. Pelton, The Li-Zn (lithium-zinc) system, J. Phase Equilib. 12 (1) (1991) 42–45.
- [34] C. Mao, Microstructure and Deformation Mechanism of Zn-Li Alloys, Chongqing University, 2018.
- [35] G.N. Li, S.M. Zhu, J.F. Nie, Y. Zheng, Z. Sun, Investigating the stress corrosion cracking of a biodegradable Zn-0.8 wt%Li alloy in simulated body fluid, Bioact. Mater. 6 (5) (2021) 1468-1478.
- [36] C. Chen, H. Huang, J. Niu, J. Nie, G. Yuan, Origin of high tension-compression yield asymmetry in as-extruded pure zinc, Scr. Mater. 200 (2021) 113922.
- [37] Y. Murakami, T. Takagi, K. Wada, H. Matsunaga, Essential structure of S-N curve: Prediction of fatigue life and fatigue limit of defective materials and nature of scatter, Int. J. Fatigue 146 (2021) 106138.
- [38] ASM Handbook, Volume 12, ASM International, Fractography, 1987.
- [39] S. Huang, W. Wu, Y. Su, L. Qiao, Y. Yan, Insight into the corrosion behaviour and degradation mechanism of pure zinc in simulated body fluid, Corros. Sci. 178 (2021) 109071.
- [40] Z. Gao, X. Zhang, H. Huang, C. Chen, J. Jiang, J. Niu, M. Dargusch, G. Yuan, Microstructure evolution, mechanical properties and corrosion behavior of biodegradable Zn-2Cu-0.8Li alloy during room temperature drawing, Mater. Charact. 185 (2022) 111722.
- [41] R. Naseri, H. Hiradfar, M. Shariati, M. Kadkhodayan, Corrosion-fatigue resistance of ultrafine grain commercially pure titanium in simulated body fluid, Proc. Inst. Mech. Eng. Part E 0 (0) (2022) 09544089221140682.
- [42] Y. Uematsu, C.A. Huang, T. Kakiuchi, Y. Mizutani, M. Nakajima, Effect of heat treatment at the temperature above β-transus on the microstructures and fatigue properties of pure Ti, Fatigue Fract. Eng. Mater. Struct. 43 (12) (2020) 2800–2811.
- [43] K.V. Mjali, Fatigue life prediction of laser and mechanically formed commercially pure grade 2 titanium alloy plates, Procedia Manuf. 48 (2020) 256–266.
- [44] M. Áman, K. Wada, H. Matsunaga, H. Remes, G. Marquis, The influence of interacting small defects on the fatigue limits of a pure iron and a bearing steel, Int. J. Fatigue 135 (2020) 105560.
- [45] M. Liu, J. Wang, S. Zhu, Y. Zhang, Y. Sun, L. Wang, S. Guan, Corrosion fatigue of the extruded Mg-Zn-Y-Nd alloy in simulated body fluid, J. Magn. Alloys 8 (1) (2020) 231-240.
- [46] S. Wackenrohr, C.J.J. Torrent, S. Herbst, F. Nürnberger, P. Krooss, C. Ebbert, M. Voigt, G. Grundmeier, T. Niendorf, H.J. Maier, Corrosion fatigue behavior of electron beam melted iron in simulated body fluid, npj Mater. Degrad. 6 (1) (2022) 18.